3 The LHC machine and experiments

A. Alici[a], *M. Bomben*[b], *I. Dawson*[c], *J. Sonneveld*[d]
[a]University of Bologna, Italy
[a]LPNHE & University of Paris, France
[c]Queen Mary University of London, United Kingdom
[d]Nikhef, Amsterdam, Netherlands

The Large Hadron Collider is a 26.7 km circular accelerator based on a twin aperture superconducting magnet design with a design proton beam energy of 7 TeV [1]. The four particle physics experiments ALICE, ATLAS, CMS, and LHCb are located at the positions indicated in Fig. 12.

The LHC was first operated with beams for short periods in 2008 and 2009. In 2010, a first experience with the machine was gained at a beam energy of 3.5 TeV, with moderate beam intensities of 1.1×10^{11} protons per bunch (ppb) and up to $\sim$200 bunches. In 2011, the beam intensity was increased to $\sim$ 1400 bunches of 1.4×10^{11} ppb, while 2012 was dedicated to luminosity production with higher bunch intensities (1.6×10^{11} ppb) and a beam energy of 4 TeV. The running years 2010–2013 are commonly referred to as Run 1. In early 2013 beam operation was stopped for a 2 year long shutdown (LS1) to complete work on the magnets in view of reaching the design beam energy. Beam operation resumed in 2015 with beam energies of 6.5 TeV following a dipole training campaign that took place at the end of LS1 [2]. The LHC experiments had expressed a strong preference for beams with 25 ns bunch spacing, as opposed to the 50 ns spacing used in 2011–2012, as this would result in too many inelastic collisions per crossing (pile-up). On the machine side, this posed additional challenges, so 2015 became a learning year dedicated to preparing the machine for full luminosity production in 2016–2018 (Run 2). Further details of machine operation during Run 2 can be found in Ref. [3].

In addition to the proton beams, one month per year is dedicated to running with heavy ions, providing either Pb–Pb or p–Pb collisions. The first two years of Run 1 provided Pb–Pb collisions to the experiments, and the final year was dedicated to p–Pb. Run 2 (2015–2018) again saw a mix of Pb–Pb and p–Pb set-ups, except in 2017- when Xe–Xe collisions were provided for the first time to the experiments.

3.1 Luminosity delivered to the experiments

The main driver of radiation backgrounds in the experiments is from the collisions, although beam backgrounds can play a role too. The rate of collisions R in an experiment is given simply by the product of the particle interaction cross-section σ_{int} and the instantaneous luminosity L:

$$R = L \times \sigma_{\text{int}}, \qquad L = \frac{kN^2 f}{4\pi\sigma_x^*\sigma_y^*}F\,, \tag{20}$$

where k is the number of colliding bunch pairs, N the particle number of each bunch, and f is the LHC revolution frequency ($=11.25$ kHz). Here, σ_x^* and σ_x^* are the horizontal and vertical beam sizes at the interaction point and F (≤ 1) is a geometric reduction factor which takes into account the reduced luminosity due to beam crossing angles at the interaction point.

Shown in Fig. 13 is the delivered integrated luminosity in 2018 for all four LHC experiments. The delivered luminosity is the important quantity for radiation background considerations, and not the ‘recorded’ luminosity, which is when the experiment starts taking data during a run. ATLAS has multiple

---

This chapter should be cited as: The LHC machine and experiments, Eds. A. Alici *et al.*, DOI: 10.23731/CYRM-2021-001.23,
in: Radiation effects in the LHC experiments: Impact on detector performance and operation, Ed. Ian Dawson,
CERN Yellow Reports: Monographs, CERN-2021-001, DOI: 10.23731/CYRM-2021-001, p. 23.

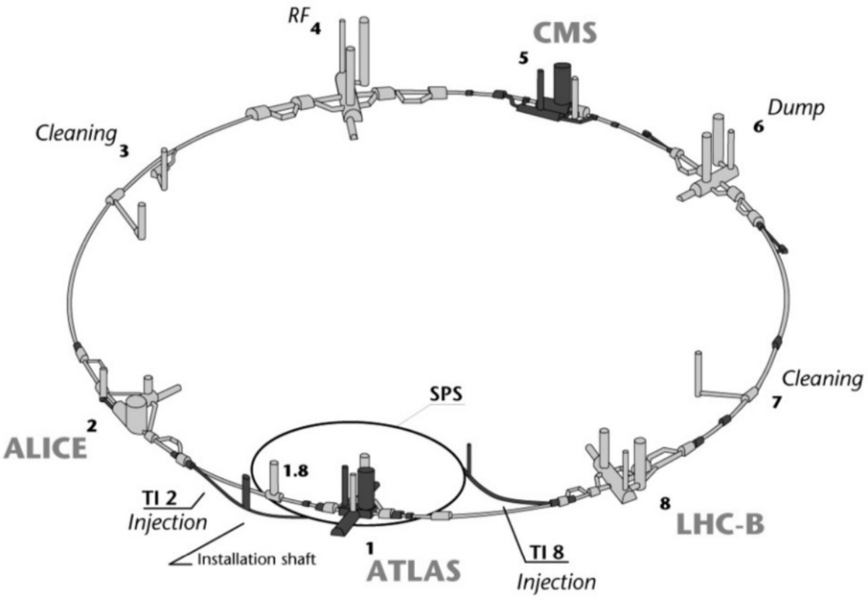

Fig. 12: The LHC layout

luminosity monitors, with the primary luminosity measurement performed by the LUCID-2 detector [4]. Additional detectors and dedicated LHC runs are used to achieve an uncertainty of 1.7% for Run 2 [5]. Similarly to ATLAS, CMS makes use of several luminosity monitors to measure the LHC delivered luminosity. All systems contribute to improve the accuracy of the measurement, reaching for the Run 2 an uncertainty of 1.8%.

The example of the total integrated luminosity delivered to the CMS experiment over the period 2010–2018 is shown in Fig. 14. The situation for ATLAS is similar. The gaps in the measurements correspond either to machine winter technical stops or the long shutdown LS1 (2013–2014). The total integrated luminosities delivered to experiments for pp, p–Pb, and Pb–Pb collisions are given in Table 1.

The particle collision rates inside the experiments are determined by the luminosity and the interaction cross-sections (Eq. 20). In particular, it is the inelastic component of the total cross-section that generates the dominant component of the radiation backgrounds in and around the LHC experiments. The particles from low angle elastic scattering disappear down the beam line, eventually interacting with elements of the machine. Measurements of the inelastic proton–proton cross-section have now been measured by all the experiments, and an example of how these compare for different centre of mass energies is given in Fig. 15. The ATLAS measured value at $\sqrt{s}$ = 13 TeV is 78.1 ± 2.9 mb.

Table 1: Total integrated luminosities delivered to each of the experiments for the different particle collisions.

	pp ($\mathbf{fb^{-1}}$)		**Pb–Pb ($\mathbf{nb^{-1}}$)**		**p–Pb ($\mathbf{nb^{-1}}$)**	
	Run 1	**Run 2**	**Run 1**	**Run 2**	**Run 1**	**Run 2**
ATLAS	28.0	157.0	0.176	2.37	31.2	183.8
CMS	29.4	162.9	0.184	2.49	36.14	188.3
LHCb	3.47	6.35	-	0.24	2.14	34.1
ALICE	0.015	0.067	0.153	1.34	31.9	43.3

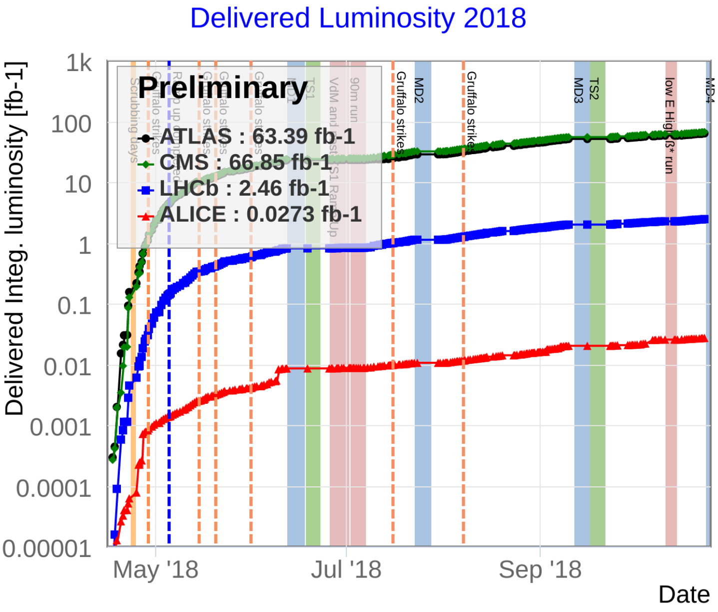

Fig. 13: LHC delivered integrated luminosity in 2018 for all four LHC experiments. The luminosity of ALICE was levelled to achieve moderate collision rates. Figure from Ref. [6].

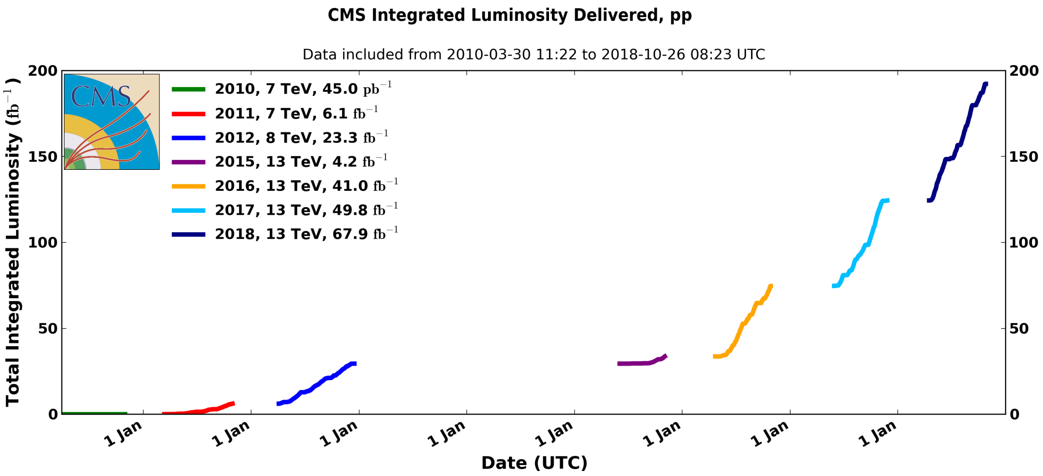

Fig. 14: CMS cumulative integrated luminosity versus day delivered to CMS during stable beams for pp collisions at nominal centre of mass energy. The CMS strip tracker has seen a total of 192.3 fb^{-1}; the original CMS pixel detector was exposed to 74.6 fb^{-1}, the Phase-1 pixel detector, installed in 2017, has seen 117.7 fb^{-1}. Figure from Ref. [7].

3.2 The large LHC experiments

The LHC hosts a multitude of experiments. This report focuses on the four largest, namely ALICE, ATLAS, CMS, and LHCb. The inner tracking system of each of these experiments described below is affected most by radiation damage. All experiments use a right-handed coordinate system with its origin at the nominal interaction point (IP) of each of the experiments and the z-axis coincides with the axis of the beam pipe. The x-axis points from the IP towards the centre of the LHC ring, and the y-axis points upward. Cylindrical coordinates (r,ϕ) are used in the transverse plane, ϕ being the azimuthal angle around the z-axis. The pseudorapidity is defined in terms of the polar angle θ as $\eta = -\ln\tan(\theta/2)$.

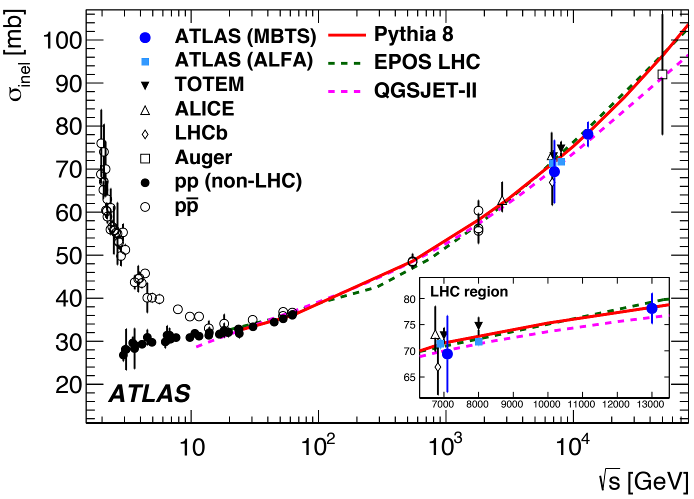

Fig. 15: Measurements and predictions of the inelastic proton–proton cross-sections. Figure from Ref. [8].

3.2.1 ATLAS

The ATLAS detector [9] was built and installed at the LHC interaction point 1 in the years 2000 to 2008. Since November 2009, when LHC first became operational, the experiment has collected 185 fb^{-1} of proton–proton collisions at 7, 8, and then 13 TeV centre of mass energy. The inner detector (ID) was designed to provide hermetic and robust pattern recognition, excellent momentum resolution, and both primary and secondary vertex measurements for charged tracks within the pseudorapidity range $|\eta| < 2.5$. The ID layout, described in Ref. [9], reflects the performance requirements: the ID is contained within a cylindrical envelope of length 3512 mm and of radius 1150 mm, within a solenoidal magnetic field of 2 T. The ID consists of three independent but complementary subdetectors: at inner radii, high-resolution pattern recognition capabilities are available using discrete space points from the silicon Pixel detector ($r < 122.5$ mm) and stereo pairs of silicon microstrips from the semiconductor tracker (SCT) ($299 < r < 514$ mm); at larger radii ($563 < r < 1066$ mm), the transition radiation tracker (TRT) comprises several layers of gaseous straw tube elements interleaved with transition radiation material.

The performance of the ATLAS experiment depends critically on the innermost layer of the Pixel detector. For this reason, at the beginning of 2013, during the LS1, a fourth pixel layer was added to the Pixel detector. Based on a new technology, the insertable B-layer (IBL) [10] was inserted between a new, narrower beryllium beam pipe and the pre-existing Pixel B-layer (the former innermost layer). Figure 16 shows the $r - z$ layout of the upgraded ID before the start of Run 2. At the same time, the Pixel services were replaced by new ones (new Service Quarter Panel, or nSQP upgrade), making repairs of the opto-electrical converters possible without extraction of the Pixel detector in the future.

After resuming data taking in 2015, ATLAS has successfully operated the ID during Run 2 at $\sqrt{s} = 13$ TeV and instantaneous luminosities surpassing the design value of $1 \times 10^{34}\,\text{cm}^{-2}\text{s}^{-1}$. The total integrated luminosity collected till 2019 by the Pixel, SCT, and TRT detectors is $\sim 190\ \text{fb}^{-1}$ whilst the IBL detector, operating only during Run 2, collected a luminosity of $\sim 159\ \text{fb}^{-1}$. The ATLAS SCT received a maximum fluence of $\Phi_{\text{eq}} \sim 4.5 \cdot 10^{13}/\text{cm}^2$ in its innermost layer, whereas the ATLAS pixel detector received a factor 20 more fluence $\Phi_{\text{eq}}, \sim 1 \cdot 10^{15}/\text{cm}^2$.

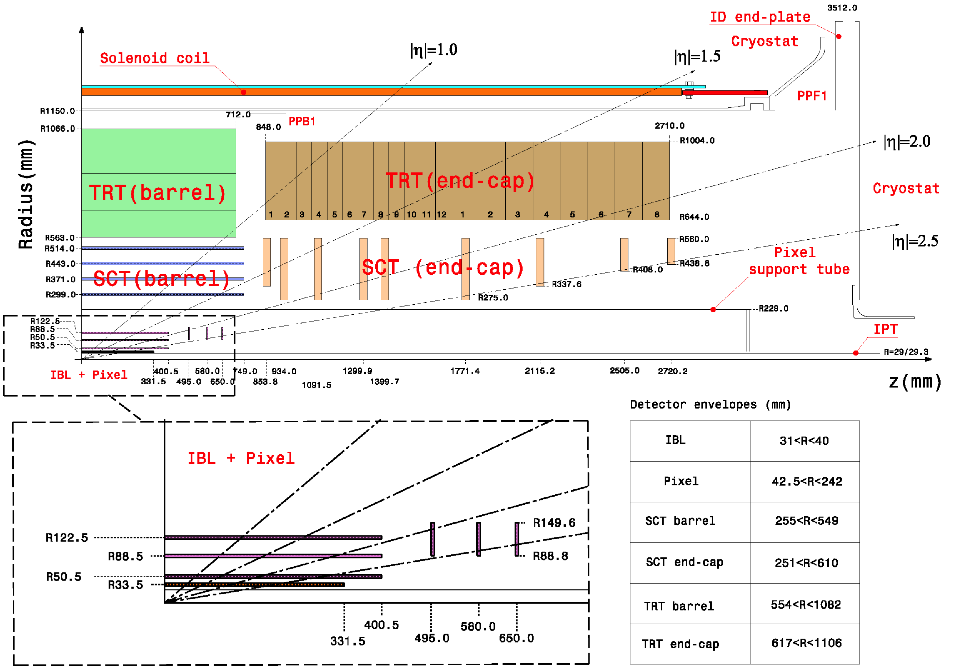

Detector envelopes (mm)

IBL	31<R<40
Pixel	42.5<R<242
SCT barrel	255<R<549
SCT end-cap	251<R<610
TRT barrel	554<R<1082
TRT end-cap	617<R<1106

Fig. 16: Layout of the ATLAS inner detector, including the IBL installed before LHC Run 2. The top panel shows the whole inner detector, whereas the bottom panel shows a magnified view of the Pixel detector.

3.2.1.1 *The ATLAS pixel detector*

The ATLAS pixel detector [10–12] consists of four barrel layers and a total of six disc layers, three at each end of the barrel region. The four barrel layers are composed of n^+-in-n planar oxygenated [13, 14] silicon sensors (p-type implants in n-type silicon) at radii of 33.5, 50.5, 88.5, and 122.5 mm from the geometric centre of the ATLAS detector. The IBL sensors are 200 μm thick while the sensors in the other layers are 250 μm thick. At high $|z|$ on the innermost barrel layer, there are n^+-in-p 3D sensors [15] that are 230 μm thick. The IBL pixel pitch is $50 \times 250\,\mu\text{m}^2$; everywhere else the pixel pitch is $50 \times 400\,\mu\text{m}^2$. The IBL is cooled with two-phase CO_2 cooling [16] with a nominal set temperature of $-20\,°C$. The sensors are around $-13\,°C$ with the front-end electronics powered during data taking. Charged particles traversing the sensors deposit energy by ionizing the silicon bulk; for typical LHC energies, such particles are nearly minimum-ionizing particles (MIP). The deposited charge drifts through the sensor and the analogue signal recorded by the electrode is digitized, buffered, and read out using an FE-I4B [17] (IBL) or FE-I3 [12] (all other layers) chip.

3.2.1.2 *The ATLAS SCT detector*

The ATLAS SCT consists of four concentric silicon strip barrel layers, and two endcaps, each with nine disks, as indicated in Fig. 16. All the silicon strip sensors are 285 mm thick and are constructed of high-resistivity n-type bulk silicon with p-type implants. The barrel system is built from 2112 modules [18], and each endcap from 988 modules. Barrel modules consists of four rectangular silicon-strip sensors [19] with strips with a constant pitch of 80 mm. The SCT has a particle rapidity coverage of $|\eta| < 2.5$. Each barrel or disk provides two strip measurements at a stereo angle which are combined to build space-points. The SCT typically provides eight strip measurements (four space-points) to reconstruct particles coming from the proton-proton interactions.

3.2.1.3 *The ATLAS TRT detector*

The main detector component of the TRT is a cylindrical 4 mm diameter straw of thin-wall proportional chamber. Charged particles passing through the straw cause ionization of the gas atoms by exchange of either virtual photons from Coulomb interactions or real photons from transition radiation created in radiator material surrounding the straw. The liberated electrons drift according to the electric field applied, and are collected by the centre anode wire in the straw. The secondary electron drift time ranges up to 70 ns depending on the distance from a hit to the wire. The detector consists of a barrel and two endcaps; the barrel has 52 544 axial straws of about 144 cm length with anode wires read out by both ends independently; the endcaps situated on both sides of the barrel contain 122 880 straws each; giving 350 848 straws in total.

3.2.2 *CMS*

The Silicon Tracker of the Compact Muon Solenoid (CMS) [20] is the largest silicon tracker in the world. It is operated in a magnetic field of 3.8 T and reconstructs charged particle trajectories (tracks) that originate from the proton–proton collisions delivered by the LHC. The CMS tracker consists of a hybrid pixel detector as innermost part and a silicon strip tracker at larger radii. The CMS pixel detector [21] (also called the Phase-0 pixel detector) was running during the years 2009–2012 and 2015–2016 and was replaced with the CMS Phase-1 pixel detector [22] during the extended year-end technical stop 2016–2017. The strip tracker and the Phase-0 pixel detector cover(ed) the pseudo-rapidity range $|\eta| < 2.5$, the coverage of the Phase-1 pixel detector extends up to $|\eta| = 3.0$. A schematic of the CMS tracker is shown in Fig. 17.

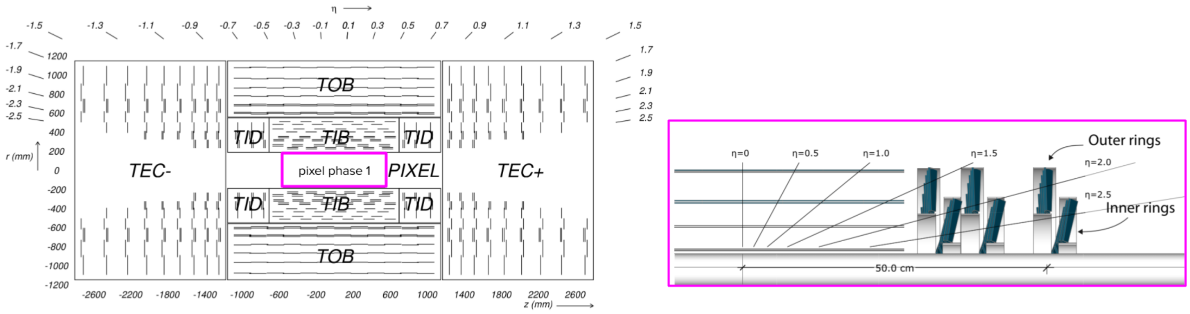

Fig. 17: The layout of the CMS tracker. Left: overview of the entire CMS tracker, with the CMS strip tracker detailed. It consists of 10 barrel layers and 12 disks on each detector end. Right: the layout of the CMS Phase-1 pixel detector that was installed in 2017. It consists of 4 layers and 3 endcap disks on each detector end. Figures from Ref. [22].

3.2.2.1 *The CMS pixel detector*

The pixel Phase-1 (Phase-0) system consists of a barrel part with four (three) layers and two endcaps with three (two) disks each on either side of the interaction point. The pixel detector uses 285 μm thick n^+ in n sensors with 100×150 μm^2 pixels. The sensors are bump bonded to the readout chips (ROC). Its innermost layer is located 2.9 cm (4.4 cm for the Phase-0 detector) from the beamline. At this distance the particle rates reach 600 MHz/cm^2 and the dose and fluence reach in excess of 100 Mrad or $1 \times 10^{15} n_{eq}$, respectively over the lifetime of the detector.

The detector modules were read out by the PSI46 chip in the original detector and by the PSI46dig [23, 24] for the upgraded detector apart from the innermost barrel layer, which is read out by the PROC600 ASIC [25], specifically designed to cope with the very high particle rates in this region.

Table 2: Operational bias voltages and maximum fluence for the CMS pixel detector at $z = 0$ in the barrel and the module part closest to the beam line for the endcaps at the end of Run 2 in 2018. The distance from the beam line is also shown. This distance varies over modules on rings in the endcaps. The fluence variation in the endcaps results from the different distances in z from the interaction point of the 3 disks on each end of the detector.

Layer/ring	Operational bias	Radius	Maximum fluence Φ_{eq}
layer 1	450 V	2.9 cm	$7.9 \times 10^{14}/\mathrm{cm}^2$
layer 2	300 V	6.6 cm	$1.8 \times 10^{14}/\mathrm{cm}^2$
layer 3	250 V	10.9 cm	$9 \times 10^{13}/\mathrm{cm}^2$
layer 4	250 V	16.0 cm	$5 \times 10^{13}/\mathrm{cm}^2$
ring 1	350 V	4.5–11 cm	2.92–$3.32 \times 10^{14}/\mathrm{cm}^2$
ring 2	300 V	9.5–16 cm	1.09–$1.15 \times 10^{13}/\mathrm{cm}^2$

The other components of the pixel module are the high-density interconnect (HDI) printed circuit and the token bit manager (TBM) ASIC [26]. The ROCs read out the individual pixels in a double-column structure with a global threshold per ROC. The TBM controls the programming and orchestrates the readout of the ROCs upon the receipt of a Level-1 accept (L1A) signal by passing a readout token to the group of ROCs it is connected to. Most of the auxiliary electronics for the pixel detector are located on the service cylinders outside of the active detector volume. Module power is regulated with DCDC converters [27] using the CERN FEAST2 ASIC [28] that is controlled with command and control units (CCUs) [29] similar to those used in the CMS strip tracker (see below). A detailed description of the CMS Pixel DAQ is given in Ref. [30]

The sensors of the Phase-1 pixel detector are cooled with bi-phase CO_2 cooling [31–33] at a temperature of $-22\,°C$. The effective temperature on the carbon fibre support structure of the modules ranges from -14 to $-8\,°C$ when the modules are powered ($-18\,°C$ when unpowered), with higher temperatures at the start and lower temperatures at the end of cooling loops.

The original CMS pixel detector was exposed to $74.6\,\mathrm{fb}^{-1}$ while the Phase-1 detector has seen $117.7\ \mathrm{fb}^{-1}$. The operational bias voltage in the pixel system is adjusted during the run to compensate the effects of radiation. This is done taking into account the fluence a detector part has been exposed to. The operational voltage and approximate fluence for the individual detector parts is summarized in Table 2.

3.2.2.2 The CMS strip detector

The CMS strip tracker contains 15 148 modules with more than 9.3 million silicon strips covering a total active area of silicon of $198\,\mathrm{m}^2$. It is organized in large substructures: the inner barrel (TIB) with four layers, the inner disks (TID) with three disks on each end of the TIB volume in the forward region, the outer barrel (TOB) which completely surrounds the TIB and TID and consists of 6 layers, and the two large endcaps (TEC) with 9 disks each that complement the strip tracker on either side of the interaction point. The first two layers of the TIB and TOB and rings 1 and 2 (1, 2, and 5) of the TIB(TEC) contain stereo modules with silicon modules mounted back to back for 3D space point reconstruction. The strip tracker sensors are of n-type silicon with 512 or 768 p^+ single-sided strips with a thickness of $320\,\mu$m up to a radius of 600 mm, and $500\,\mu$m at larger radii. The charge on each microstrip is read out and amplified by a $0.25\,\mu$m analogue pipeline voltage (APV25) chip [34]. A module contains either 4 or 6 APV25 chips. The APV chips are located on the so-called front-end hybrid which also houses auxiliary chips like a multiplexer (APVMUX), a PLL chip and a detector control unit (DCU) which allows readout of slow-control monitoring data like low voltage levels, temperatures, and the leakage current of the silicon sensors. The module is connected via a cable to the analogue-opto hybrid (AOH) which houses a linear laser driver (LLD). The control of the detector modules happens through token or control-ring

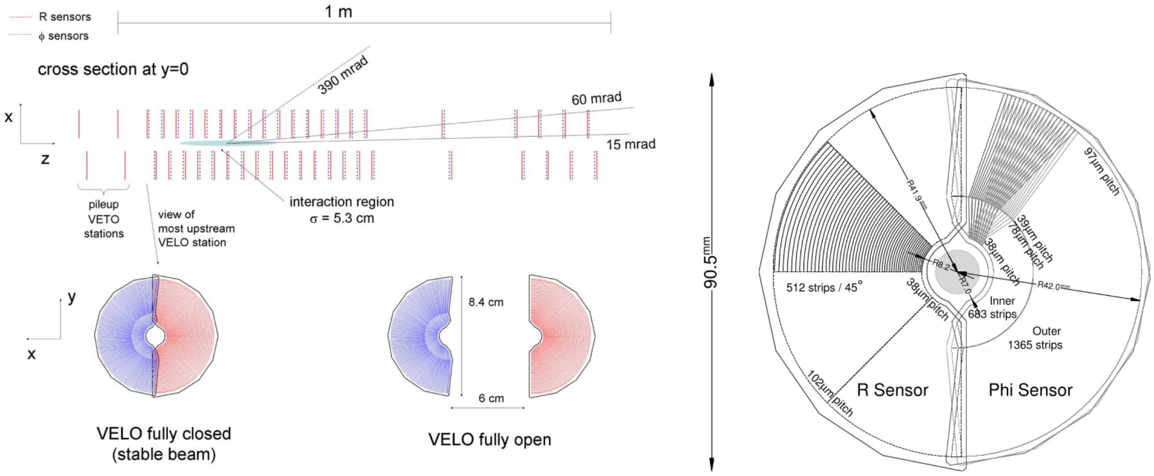

Fig. 18: Left top: cross-section of the LHCb VELO modules when fully closed around the beam line at $y = 0$. Left bottom: front face of first VELO modules when VELO is fully closed (left) and fully opened (right). Right: the different types of sensors in the LHCb VELO detector. Figures from Ref. [35].

networks of clock and control units (CCU). The token rings are connected via bidirectional optical links to the front-end controllers (FEC) located in the service cavern outside the radiation zone. The FECs send clock, trigger, and fast commands to the modules and transmit configuration data to them. The link allows for a readback of the configuration parameters and the communication with the DCU.

Upon receipt of an L1A the charge of a pipeline cell is read out by an analogue pulse shape processor (APSP) that can operate in two modes. In *peak mode* a single cell is read out, timed to be at the peak of the analogue pulse. In *deconvolution mode*, three samples are read out and the output is the weighted sum of all three. The shaper of the APV has a pulse shape with a length of 200 ns which is much longer than the LHC bunch spacing of 25 ns. In deconvolution mode the pulse is reshaped to peak after 25 ns resulting in a pulse length of about 50 ns; this happens at the expense of increased noise. The signal from two chips is time multiplexed in the APVMUX and converted to an optical signal on the AOH. The signal is then transferred via optical fibres of 60–100 m length to the service cavern to the front-end drivers (FED).

The strip tracker uses a mono-phase C_6F_{14} cooling system. The coolant temperature was $+4°C$ during Run 1 and was lowered to $-15°C$ during the running years 2015–2017 and to $-20°C$ during 2018.

3.2.3 LHCb

The LHCb tracking system (Run 1 and Run 2) is comprised of two silicon detectors, the LHCb vertex locator (VELO), and the silicon tracker (ST) [35]. The LHCb VELO detector consists of two retractable halves, each with 21 modules containing a pair of n-on-n silicon sensors of 300 μm thickness. A cross-section of the VELO modules when closed in around the beam line is shown on the left in Fig. 18.

Each module contained two sensor types, R-type sensors with 2048 concentric strips and ϕ-type with 2048 radial strips as shown on the right in Fig. 18. The innermost active channels were placed at approximately 8 mm from the proton beams during the stable data taking conditions.

The sensor pitch ranged from 35 μm closest to the beam line to 101 μm furthest away from the beam line. Strip isolation was achieved through p-spray and a minimum pitch of 35 μm for the sensors at the innermost radius for optimal vertex resolution.

The VELO detector is operated in a secondary vacuum, separated from the primary LHC vacuum by a 300 μm thick aluminium radio-frequency (RF) foil. It is cooled with two-phase CO_2 cooling with a nominal set temperature of $-30\,^\circ$C. The sensors are at around $-8\,^\circ$C with the front-end electronics powered during data taking.

The vertex locator has operated since the start of the LHC and has since collected 3 fb^{-1} of proton–proton collision data in Run 1 and 9 fb^{-1} in Run 2. With their proximity to the beam line at a distance of only 8 mm, the innermost VELO sensors have been exposed fluences up to about $\Phi_{\mathrm{eq}} \sim 6.5 \times 10^{14}/\mathrm{cm}^2$.

The ST is part of the LHCb main tracking system which consists of four tracking stations, one upstream and three downstream of the LHCb dipole magnet. The trigger tracker or tracker turicensis (TT) constitutes the first tracking station while the inner tracker (IT) covers and cross-shaped region around the beam pipe in the three downstream tracking stations. The TT is a planar station with dimensions about 130 cm in height and 150 cm in width. The IT is about 120 cm wide and 40 cm high. Both the IT and TT have four silicon detection layers using silicon microstrip sensors. The first and last layer of each station has the strips in the vertical direction. The two middle layers of each station have a stereo angle compared to the vertical with the first station rotated by -5° and the third station by $+5^\circ$. The TT uses 500 μm p^+-in-n sensors with a strip pitch 183 μm. The IT uses p^+-in-n sensors with a strip pitch of 198 μm. The modules in the horizontal plane have 410 μm thickness and a strip length of 22 cm through daisy chaining of two individual sensors. The sensors at the top and bottom are of 320 μm. In the latter case a single sensor is used resulting in a strip length of 11 cm.

3.2.4 ALICE

The ALICE inner tracking system (ITS) [36] operated in Run 1 and Run 2 consisted of six cylindrical layers of silicon detectors placed coaxially around the beam pipe, based on different technologies, and located at radii between 3.9 and 43 cm (Fig. 19). It provided a rapidity coverage $|\eta| < 0.9$ for all vertices located within the length of the interaction diamond ($\pm 1\sigma$, i.e., ± 5.3 cm along the beam direction). The number, position, and segmentation of the layers were optimized for efficient track finding and high impact parameter resolution. In particular, the inner radius is the minimum allowed by the radius of the beam pipe, while the outer radius is determined by the necessity to match tracks with those from the time projection chamber (TPC).

Table 3 summarizes the main characteristics of each layer. Due to the high particle density expected in heavy-ion collisions at LHC (as many as 50 particles per cm^2 have been predicted for the inner layer), and in order to achieve the required impact parameter resolution, silicon pixel detectors (SPD) have been chosen for the innermost two layers, and silicon drift detectors (SDD) for the following two layers. The two outer layers, where the track density is expected to be below one particle per cm^2, are equipped with double-sided silicon micro-strip detectors (SSD). The four outer layers have analogue readout and therefore can be used for particle identification via $\mathrm{d}E/\mathrm{d}x$ measurement in the non-relativistic ($1/\beta^2$) region. The analogue readout has a dynamic range large enough to provide the $\mathrm{d}E/\mathrm{d}x$ measurement for low-momentum highly ionizing particles, down to the lowest momentum at which tracks can still be reconstructed. This feature gives the ITS standalone capability as a low-p_{T} particle spectrometer. The ITS provided the reconstruction of the collision point (primary vertex), with a resolution of 10 μm in central Pb–Pb collisions, and the displaced vertices (secondary vertices), with a resolution better than 100 μm [37].

3.2.4.1 The silicon pixel detector

The two innermost layers making the silicon pixel detector (SPD), were based on hybrid pixel detectors with binary output consisting of 200 μm thick silicon sensor matrix and 150 μm thick bump-bonded readout chips. The matrix had 256×160 reversely biased (50 V) p-n diodes, forming cells 50 μm wide (rϕ) and 425 μm long (z). The binary output is readout at 10 MHz. The detector is equipped with a $\mathrm{C_4F_{10}}$-based evaporative cooling system.

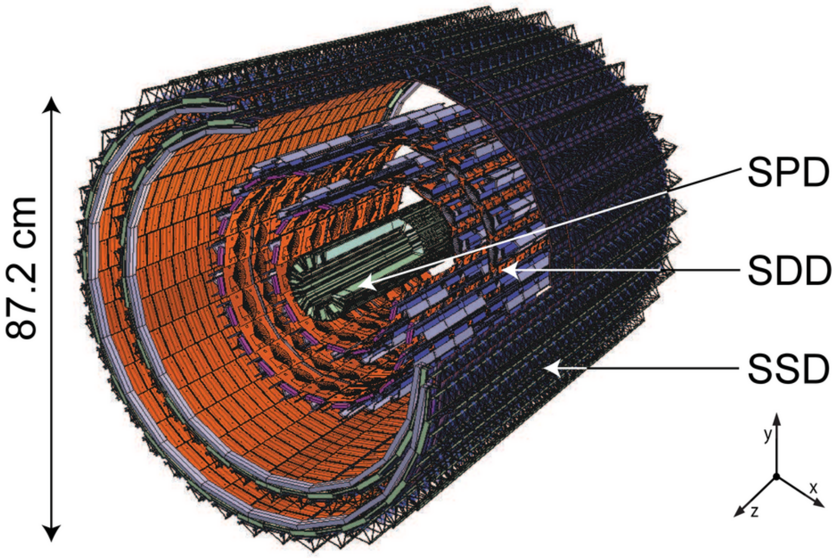

Fig. 19: The ALICE inner tracking system before 2019 from the start of the LHC up to long shutdown 2 (LS2). Figure from Ref. [36].

Table 3: Characteristics of the ITS, layer by layer. Res. is the resolution, along the bending direction (rϕ) and the beam axis (z). M.B. is the material budget, expressed in terms of radiation lengths (X_0).

Layer	**Detector**	**Radius**	**Length**	**Channels**	**Area**	**Res. (μm)**		**M.B.**
		(cm)	**(cm)**		**(m^2)**	**rϕ**	z	**(% X_0)**
1	SPD	3.9	28.2	3.3 M	0.07	12	100	1.14
2		7.6	28.2	6.5 M	0.14			1.14
3	SDD	15.0	44.4	43 k	0.42	35	25	1.13
4		23.9	59.4	90 k	0.89			1.26
5	SSD	38.0	86.2	1.1 M	2.20	20	830	0.83
6		43.0	97.8	1.5 M	2.80			0.83

3.2.4.2 *The silicon drift detector*

The silicon drift detector (SDD) equipped the two intermediate layers of the ITS and was based on 300 μm thick drift sensor and custom hybrid readout boards. The sensitive area of the module was divided into two drift regions along the bending direction (rϕ) by the central cathode at -1.8 kV. In each drift region and on both detector surfaces, p$^+$ cathode strips (120 μm pitch) were used to fully deplete the detector and generate a uniform electric drift field (500 V/cm), parallel to the module surface, towards collection anodes (294 μm pitch) aligned with the beam axis. The drift speed was about 6.7 μm/s and was monitored by means of MOS charge injectors. The analogue SDD information was digitized by 10-bit ADCs at 20 MHz at the level of the front-end electronics developed on CMOS 0.25 μm. The SDD was equipped with a leakless water cooling system.

3.2.4.3 *The silicon strip detector*

The two outermost layers of the ITS consisted of double-sided strip sensors, with a thickness of 300 μm, connected with two HAL25 front-end chips, making the silicon strip detector (SSD). The analogue signals were digitized by 12-bit ADCs directly in the readout electronics placed outside the ALICE solenoid magnet. The p$^+$n reverse bias was optimized in the range 20–80 V. The SSD was provided with a leakless water cooling system shared with the SDD, and, due to the sensitivity of the detector to the air humidity, an air dryer system was also used to keep the absolute humidity between 1 and 1.5 g/kg.

Because of lower collision rates, the ALICE ITS saw less fluence and dose than the ATLAS, CMS, and LHCb detectors. The fluence and dose seen by the ALICE ITS subsystems in Run 1 and Run 2 are summarized in Table 4 for the innermost layer of each system.

Table 4: ALICE fluence and dose levels after Run 1 and Run 2 at the end of 2018 in its inner tracking system (ITS). Only the maximum fluence of the innermost layer of each subsystem is shown.

ITS subdetector	Radius	Maximum TID	Maximum hadron fluence Φ_{eq}
SPD	3.9 cm	19.3 krad	$3.2 \times 10^{11}/\text{cm}^2$
SDD	15 cm	1.65 krad	$4.0 \times 10^{10}/\text{cm}^2$
SSD	38 cm	0.37 krad	$1.8 \times 10^{10}/\text{cm}^2$

References

[1] O.S. Brüning *et al.* (Eds.), LHC design report, CERN-2004-003-V-1 (CERN, Geneva, 2004), doi:10.5170/CERN-2004-003-V-1.

[2] A. Verweij, Circuit performance at 6.5 TeV and beyond, LHC Performance Workshop, Chamonix,France, 2016, Indico.

[3] J. Wenninger, *PoS* **CHARGED2018** (2019) 001, doi:10.22323/1.339.0001.

[4] G. Avoni *et al.*, *JINST* **13** (2018) P07017, doi:10.1088/1748-0221/13/07/P07017.

[5] ATLAS Collaboration, Luminosity determination in pp collisions at $\sqrt{s} = 13$ TeV using the ATLAS detector at the LHC, ATLAS-CONF-2019-021 (CERN Geneva, 2019).

[6] LHC Program Coordination Performance plots for pp collisions, May–Sep 2018.

[7] CMS Collaboration, CMS luminosity public results.

[8] ATLAS Collaboration *Phys. Rev. Lett.* **117** (2016) 182002, doi:10.1103/PhysRevLett.117.182002.

[9] ATLAS Collaboration, *JINST* **3** (2008) S08003, doi:10.1088/1748-0221/3/08/S08003.

[10] ATLAS Collaboration, ATLAS insertable B-layer: technical design report, CERN-LHCC-2010-013, ATLAS-TDR-19 (CERN, Geneva, 2010).

[11] ATLAS Collaboration, *JINST* **13** (2018) T05008, doi:10.1088/1748-0221/13/05/T05008.

[12] ATLAS Collaboration, *JINST* **3** (2008) P07007, doi:10.1088/1748-0221/3/07/P07007.

[13] ROSE Collaboration, 3rd RD48 status report: the ROSE collaboration (R&D on silicon for future experiments), CERN-LHCC-2000-009 (CERN, Geneva, 2000).

[14] ROSE Collaboration, *Nucl. Instrum. Methods Phys. Res.* **A465** (2000) 60, doi:10.1016/S0168-9002(01)00347-3.

[15] S.I. Parker, C.J. Kenney, J. Segal, *Nucl. Instrum. Methods Phys. Res.* **A395** (1997) 328, doi:10.1016/S0168-9002(97)00694-3.

[16] B. Verlaat *et al.*, *JINST* **12** (2017) C02064, doi:10.1088/1748-0221/12/02/C02064.

[17] M. Garcia-Sciveres *et al.*, *Nucl. Instrum. Methods Phys. Res.* **A636** (2011) S155, doi:10.1016/j.nima.2010.04.101.

[18] A. Abdesselam *et al.*, *Nucl. Instrum. Methods Phys. Res.* **A568** (2006) 642, doi:10.1016/j.nima.2006.08.036.

[19] A. Ahmad *et al.*, *Nucl. Instrum. Methods Phys. Res.* **A578** (2007) 98, doi:10.1016/j.nima.2007.04.157.

[20] CMS Collaboration, The CMS tracker system project : technical design report, CERN-LHCC-98-06, CMS-TDR-5 (CERN, Geneva, 1998); Addendum, CERN-LHCC-2000-016, CMS-TDR-5-add-1 (CERN, Geneva, 2000).

[21] CMS Collaboration, *JINST* **3** (2008) S08004, 10.1088/1748-0221/3/08/S08004.

[22] CMS Collaboration, CMS technical design report for the pixel detector upgrade, CERN-LHCC-2012-016, CMS-TDR-11 (CERN, Geneva, 2012).

[23] H. C. Kästli, *Nucl. Instrum. Methods Phys. Res.* **A731**, (2013) 88, doi:10.1016/j.nima.2013.05.056.

[24] H. C. Kästli *et al.*, *Nucl. Instrum. Methods Phys. Res.* **A565** (2006) 188, doi:10.1016/j.nima.2006.05.038, arXiv:physics/0511166.

[25] A. Starodumov, P. Berger, M. Meinhard, *JINST* **12** (2017) C01078, doi:10.1088/1748-0221/12/01/C01078.

[26] E. Bartz, The token bit manager chip for the CMS pixel readout, Proc. Int. Workshop on Semiconductor Pixel Detectors for Particles and X-Rays (PIXEL2002), Carmel (CA), USA, Ed. S.C. Loken (SLAC, Stanford, 2002).

[27] L. Feld *et al.*, *JINST* **11** (2016) C02033, doi:10.1088/1748-0221/11/02/C02033.

[28] F. Faccio *et al.*, FEAST2: a radiation and magnetic field tolerant point-of-load buck DC/DC converter, Proc. 2014 IEEE Radiation Effects Data Workshop (REDW), Paris, France, 14–18 Jul. 2014, Eds. F. Irom, S Metzger, pp. 1–7, doi:10.1109/REDW.2014.7004569.

[29] C. Paillard, C. Ljuslin and A. Marchioro, The CCU25: a network oriented communication and control unit integrated circuit in a 0.25 μm CMOS technology, Proc. 8th Workshop on Electronics for LHC Experiments Colmar, France, Sep. 9–13, 2002, Eds. P. Sharp, C. Isabella (CERN, Geneva, 2002), pp.174–178 doi:10.5170/CERN-2002-003.174.

[30] The Tracker Group of the CMS Collaboration, *JINST* **14** (2019) P10017, doi:10.1088/1748-0221/14/10/P10017.

[31] J. Daguin *et al.*, Evaporative CO_2 cooling system for the upgrade of the CMS pixel detector at CERN, Proc. 13th InterSociety Conference on Thermal and Thermomechanical Phenomena in Electronic Systems, San Diego (CA), USA, 30 May–1 Jun. 2012, pp. 723–731, doi: 10.1109/ITHERM.2012.6231499.

[32] P. Tropea *et al.*, *Nucl. Instrum. Methods Phys. Res.* **A824** (2016), doi:10.1016/j.nima.2015.08.052.

[33] B. Verlaat, M. Van Beuzekom, A. Van Lysebetten, CO_2 cooling for HEP experiments, Proc. Topical Workshop on Electronics for Particle Physics, Naxos, Greece, 15–19 Sep. 2008, Eds. E. Dho, F. Vasey (CERN, Geneva, 2008), pp.328–336, doi:10.5170/CERN-2008-008.328.

[34] M. Raymond *et al.*, The CMS tracker APV25 0.25μm CMOS readout chip, Proc. 6th Workshop on Electronics for LHC Experiments, Krakow, Poland, 11–15 Sep. 2000 (CERN, Geneva, 2000), pp. 130–134, doi:10.5170/CERN-2000-010.130.

[35] LHCb Collaboration, *JINST* **3** (2008) S08005, doi:10.1088/1748-0221/3/08/S08005.

[36] ALICE Collaboration, *JINST* **3** 08 (2008) S08002, doi:10.1088/1748-0221/3/08/s08002.

[37] ALICE Collaboration, *Int. J. Mod. Phys.* **A29** (2014) 1430044, doi:10.1142/S0217751X14300440.